

Tripartite Detection and Sensing of Toxic Heavy Metals Using a Copper-Based Porphyrin Metal–Organic Framework

Prashanth Kannan,* Ajay Narayan Konda Ravindranath, Sunil Suresh Domala, Mitko Oldfield, Agustin Schiffrin, and Dipti Gupta



Cite This: *ACS Appl. Mater. Interfaces* 2024, 16, 64166–64176



Read Online

ACCESS |

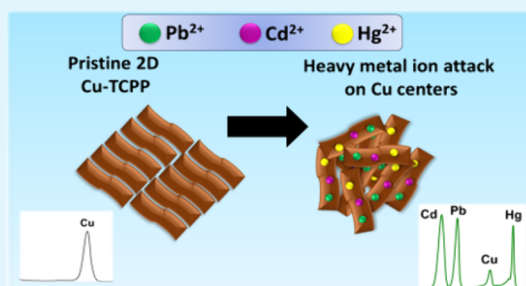
Metrics & More

Article Recommendations

Supporting Information

ABSTRACT: The detection of heavy metals in water sources is a critical concern for environmental preservation and public health. However, current electrochemical heavy metal sensors suffer from high sensing limits, cross-sensitivity, and poor selectivity. In this work, we present the possibility of an electrochemical sensor based on a copper (Cu) metal–organic framework for the detection of lead, cadmium, and mercury by replacing Cu metal nodes. The working electrode consists of a ~5 μm thin layer of copper-tetracarboxyphenylporphyrin (Cu-TCPP) sheets that are adsorbed on a glassy carbon electrode (GCE). Upon interaction with Pb^{2+} , Cd^{2+} , and Hg^{2+} , these ions are adsorbed on and incorporated into the metal nodes of the MOF. The adsorbed metallic species can be oxidized to the ionic form ($\text{Pb} \rightarrow \text{Pb}^{2+}$) electrochemically, which results in an oxidation response and enables the quantitative detection of these metals. The oxidation peak currents follow a (mostly) bimodal linear regression with a sensing range of up to 30 μM dependent on the deposition time and an ultralow limit of detection (LoD) of up to 5 nM. The system displays robust and selective sensing in saturated solutions of counterions and interfering metal ions (low error margins of <10%). This work represents the first report of a Cu-TCPP-modified GCE anode as an effective electrode for the sensitive detection of multiple heavy metals and an in-depth study into the Cu replacement kinetics of the Cu-MOF.

KEYWORDS: heavy metal sensing, Cu-TCPP, differential pulse voltammetry, metal–organic framework, electrochemical sensing



1. INTRODUCTION

Dealing efficiently with industrial effluent release and contamination—especially of toxic heavy metals (THM) discharged into waterways and landfills¹—is a major challenge in environmental science. The accumulation of THM in the environment leads to acute biotoxicity, physiological impairment, and birth defects in children and infants.² Therefore, early detection of THM accumulation is necessary to identify and flag danger zones. Extensive research has been performed in THM sensing, and several techniques such as UV–vis spectroscopy,^{3,4} ion chromatography⁵ and electrochemical analysis have been exploited to assess THM concentrations.⁶ Electrochemical techniques offer a great advantage owing to their user-friendly and efficient instrumentation, ease of parameter modification, and unique potential signatures of each heavy metal ion.⁷ Depending on the technique, impedimetric⁸ or potentiometric techniques⁹ are used to identify individual THM. Potentiometric techniques in detection are diverse, with impedimetric analysis¹⁰ and voltammetry¹¹ being the most commonly applied. Amperometric techniques typically use a single response signal to identify analyte species.¹² This leads to complexity in device design, where additional materials or structures are needed to remove interference species in the testing environment.¹³ This

can be overcome by using a ratiometric sensing method in which the responses of two signals (i.e., a reference and an analyte signal) are used. Wan et al.¹⁴ have demonstrated this using a ferrocene-doped nickel (Ni)-based metal–organic framework (MOF) to identify multiple heavy metal ions in water. In most cases, composite materials that comprise a conductive additive (e.g., carbon atoms or conductive polymers) in addition to a MOF are used to increase both the conductivity of the sensing layer and the number of active sites.¹⁵ THM accretion in soil and water induces binding with ambient metallic ions, forming intermetallic zones such as Cu–Pb, Cd–Cu, Hg–Cu, etc.³ While individual ion testing is widely available, efficient and accurate multiplex sensing of THM remains rare.

Metal–organic frameworks (MOFs) are a class of crystalline metal–organic compounds where metal ion centers are bonded to organic linkers, forming a porous network.¹⁶ This

Received: August 2, 2024

Revised: October 17, 2024

Accepted: October 23, 2024

Published: November 5, 2024



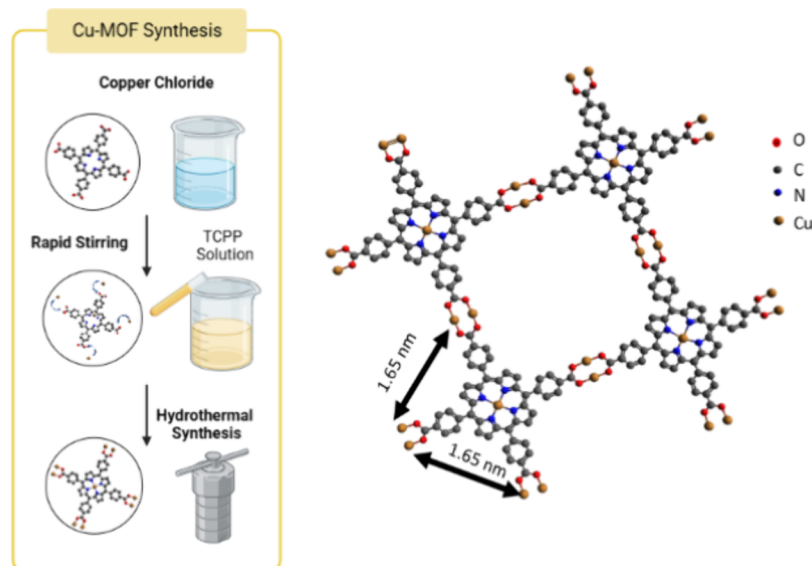


Figure 1. Schematic of the hydrothermal synthesis of Cu-TCPP MOF and chemical structure of a primitive unit cell of the formed copper MOF.

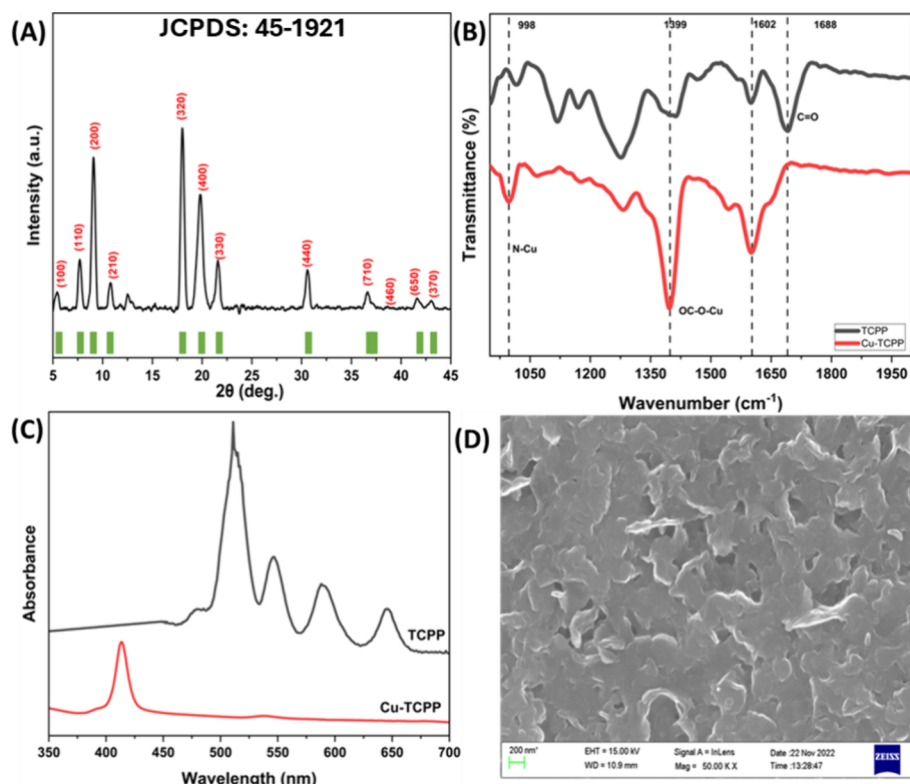


Figure 2. Structural and chemical characterization of Cu-TCPP MOF. (A) XRD spectra [5–45°] (green bars showing peak positions in JCPDS card no. 45-1921), (B) FTIR spectra [$\sigma = 400\text{--}4000\text{ cm}^{-1}$], and (C) UV-vis spectra of Cu-TCPP MOF and TCPP [$\lambda = 350\text{--}600\text{ nm}$] and (D) SEM topographical images of Cu-TCPP showing clear stacking of microplates.

confers MOFs with desirable properties such as high surface area; porosity; high density of active metal sites; and large, organized pore structures that can be modified by a change in either the metal ion or the organic linker.¹⁷ The electronic properties of MOFs are greatly affected by the changes in the environment and its constituents, which result in highly tunable band gaps, defect-induced band gap variations, and electrical conduction mechanisms.¹⁸ This has led to the extensive use of MOFs as sensor materials¹⁹; in gas storage²⁰; and as battery/supercapacitors,²¹ catalysts,²² and separator

materials.^{23,24} In the detection of THM, MOFs are extensively used to detect Cd²⁺,²⁵ Pb²⁺,²⁵ Hg²⁺,²⁷ Cu²⁺,²⁶ Fe³⁺,²⁶ and As³⁺.²⁷ Liang et al. used a Cu-based MOF HKUST-1 for the electrochemical trace detection of Pb²⁺ and Cd²⁺,²⁸ while Hu et al. used HKUST-1 for the adsorption of THM to the surface of the MOF and subsequent removal upon cycling of the electrode.

In this study, we have used a porphyrin-based Cu-MOF composed of Cu²⁺ metal centers coordinated to the terminal carboxylic groups of tetrakis(4-carboxyphenyl)porphyrin

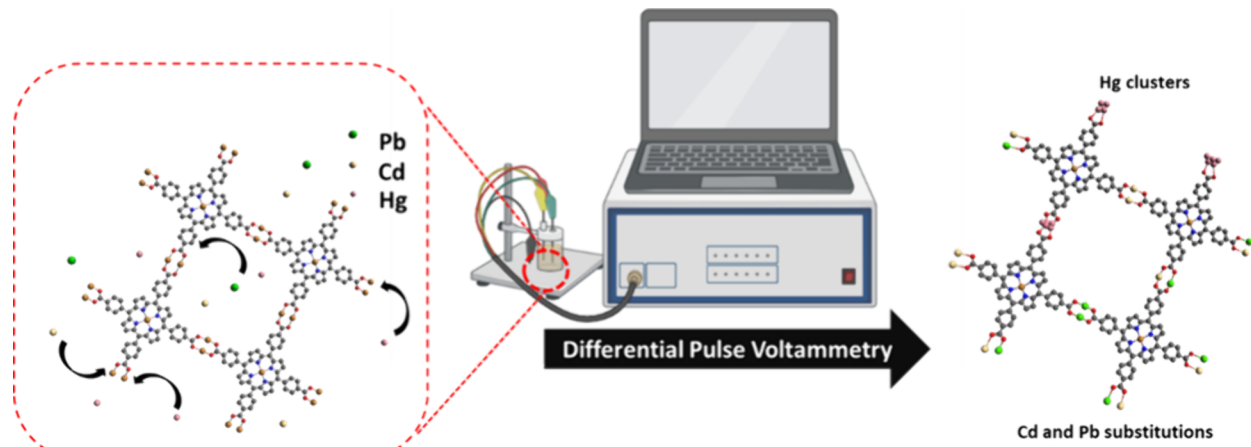
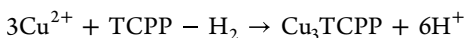


Figure 3. Illustration of heavy metal attack on copper nodes of Cu-TCPP with small Hg islands.

(TCPP) for the electrochemical sensing of heavy metal ions through differential pulse anodic stripping voltage (DPASV) techniques. To the best of our knowledge, this is the first report of Cu-TCPP being used as a heavy metal sensor this way. The hydrothermally synthesized MOF is composed of a layered nanoflake structure as seen in [Figure 1](#), which is characterized by a large surface area; this can lead to an increased interaction area in electrode applications. Heavy metal sensing and coordination are achieved when the TCPP linker liberates Cu^{2+} into the test solution. This manifests as a decrease in the copper potential and simultaneously in the emergence of specific heavy metal signatures.²⁹ Unlike conventional electrochemical sensors working through the adsorption and release of analytes, Cu-TCPP can act as a capture layer by ion exchange of Cu with THM. This work has the potential to establish multiple ion sensing capabilities (three metal ions) using one test buffer and one testing run, which has not yet been reported yet.

2. RESULTS AND DISCUSSION

2.1. Characterization. Experimental methods and synthesis are detailed in the [Supporting Information](#). The Cu-TCPP MOF has a “paddle-wheel” structure in which two copper ions form bidentate coordination between four terminal carboxyl groups of four adjacent TCPP molecules in addition to a tetradequate coordination in the porphyrin center between one copper and four nitrogen atoms. This results in large two-dimensional reticulated zones through van der Waals stacking interactions²⁹ ([Figure 1](#)). An AB stacking mode was seen to be the predominant regime from the XRD spectra ([Figure 2A](#)) according to the following reaction:



The resultant spectra indicate a higher percentage of bulk powder than nanosheets²⁹ with obvious diffraction peaks at 5.45, 7.68, 9.07, 10.78, 18.01, 19.81, 21.57, 30.55, and 36.59° representative of a vertical stacked structure. The sharp and narrow peaks denote the uniform stacking of multiple Cu-TCPP sheets when compared to the attenuated peaks that are observable in Cu-TCPP MOF nanosheets.³⁰ The FTIR spectrum, which compares the TCPP linker and the Cu-TCPP MOF, shows steep and clear transmission peaks at 1399 and 1602 cm^{-1} denoting coordination between the terminal carboxyl groups of TCPP and Cu^{2+} ions. Further proof is seen

in the weakened C=O vibration at 1688 cm^{-1} in which the TCPP disappears in the MOF ([Figure 2B](#)). The central porphyrin ligand of TCPP is also coordinated with Cu^{2+} .

This is shown by the peak at $\sim 1000 \text{ cm}^{-1}$, which proves the formation of N-Cu vibrational stretching.³¹ The UV-visible absorbance spectra of the TCPP linker shows four Soret peaks at 511, 545, 588, and 646 nm for each of the four N atoms in the porphyrin center. These peaks disappear in the Cu-TCPP MOF spectra and are replaced by two absorbance bands at 413 and 538 nm, which indicate the characteristic Soret Q bands in the metalation of the central porphyrin.³² These results prove the formation of the Cu-TCPP MOF with terminal and central Cu-coordination complexes.

The MOF surface morphology is studied using SEM, showing a stacked lamellar structure with microplates adsorbed to each other with no obvious domain formation ([Figure 2D](#)). This is characteristic of bulk stacked Cu-TCPP MOF sheets, with the flake morphology visible on the curled edges of sheets rising freely from the surface. The EDS spectra of the same were analyzed for the presence of copper, as seen in [Figure S1](#). Relative intensities of Cu, C, and O in the spectrum (4, 67, and 17%) were similar to the approximate % composition of elements expected of a Cu-TCPP MOF in a bidentate paddle-wheel configuration.

To confirm the coordination and chemical states of the Cu-TCPP MOF, high-resolution C 1s, Cu 2p, O 1s, and N 1s XPS spectra were acquired. As shown in [Figure S1](#), sharp and distinct peaks were observed for each of the elements. The deconvoluted data for C 1s show characteristic peaks at 284.9, 286.3, and 288.3, which denote C-C/C=C, C-O/C-N, and C=O/C=N, respectively ([Figure S2A](#)). Additionally, peaks at 530.6, 532.1 and 399.98, 401.9 signify the C=O, C-OH and N-Cu, N-H characteristic of the Cu-TCPP formation. The presence of spectral peaks at 935.53 (Cu 2p_{3/2}), 955.96 (Cu 2p_{1/2}), 530.5 (Cu-O), and 536.8 (C-O/O-H) serves as proof of the formation of $\text{Cu}_2(\text{COO})_4$ paddle-wheel coordination. The formation of Cu^+ was also observed due to the deconvoluted peaks at 933.23 and 953.32. The N 1s spectra in [Figure S1D](#) also show the presence of N-Cu (399.93) and N-H (401.86), which proves the central nitrogen coordination of Cu with nitrogen in the porphyrin ring; this is consistent with the FTIR results in [Figure 2B](#).³³

2.2. Electrochemical Characterization. The spectroscopy of CV and EIS was performed in an acetate buffer (pH = 5, 0.1M) and varied with the scan rate to determine the nature of

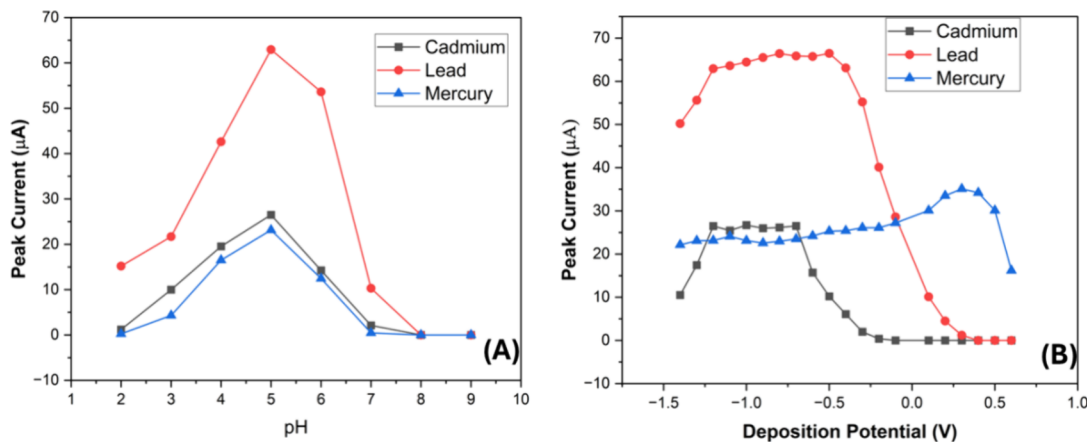


Figure 4. Variation of peak currents for 1 μM concentration of each heavy metal ion with increasing pH (A) and deposition potential (B).

the analyte–surface interaction, which is given by the Randles–Sevick equation below (i_p = peak current, n = number of electrons involved in the redox reaction, F = Faraday constant, R = gas constant, T = temperature, v = scan rate, A = electrode area, and Γ = surface coverage of adsorbed species):

$$i_p = \left(\frac{n^2 F^2}{4RT} \right) \times v \times A \times \Gamma$$

Figure S2A shows a uniform cyclic voltammogram with one oxidation and two reduction peaks that correspond to $\text{Cu} \rightarrow \text{Cu}^{2+} + 2\text{e}^-$, $\text{Cu}^{2+} \rightarrow \text{Cu} + 2\text{e}^-$, and $\text{Cu}^+ \rightarrow \text{Cu} + \text{e}^-$, respectively. A comparison of the peak currents with the scan rate shows a linear correlation with the fact that adsorbed species are the dominant interaction mechanism. The increasing peak potentials with varying scan rates corroborate this observation.³⁴

Nyquist plots of the Cu-TCPP electrode in acetate buffers of varying pH values were fitted to a simplified Randles circuit that consisted of the series resistance (R_s), the charge-transfer resistance (R_{ct}), and a constant-phase element. Minima were formed by R_{ct} at pH 5 due to the reduction of the charged double layer (Stern layer) on the electrode surface, which indicates the optimal value of the buffer for further experiments (Figure S3D). Figure 3 shows an illustration of the setup used for testing the deposition profiles of heavy metals in the Cu-TCPP-modified electrode.

The THM ions are adsorbed to the active electrode using DPASV in three steps: (1) an initial cleaning step at a positive potential (1 V), (2) a deposition step at a negative potential (-1.2 V), and (3) a sweeping scan from negative to positive potential.

Figure 3 represents a simplified view of the heavy metal replacement of Cu^{2+} sites in the Cu-TCPP MOF lattice. Three electrochemical steps are involved in the analysis to encourage the replacement of copper nodes: (1) An initial “cleaning” step done at $V = 1\text{ V}$ for 15 s, (2) a second “deposition” step at $V = -1.2\text{ V}$ for 100–250 s, and (3) a final “stripping” step where a voltammetric scan is run from -1.2 to 1 V stripping away all metals from the MOF. Considering the ionic radii of the metals involved here ($\text{Cu}^{2+} = 80\text{ pm}$; $\text{Pb}^{2+} = 118\text{ pm}$; $\text{Cd}^{2+} = 98\text{ pm}$; and $\text{Hg} = 110, 116$, and 128 pm depending on valency), replacement of Cu^{2+} sites by each of these heavy metals is possible via an ionic replacement reaction due to the similarity of ionic radii. One needs to note that Hg with its

variable valency tends to favor agglomeration. These inferences are supported by experimental data in the results.

3.3. Optimization of DPASV Parameters. DPASV is a highly sensitive procedure with variations dependent on the process parameters. Here, we have optimized the essential parameters to obtain the highest overall response. As seen in Figure 4A, the DPASV peak intensities for 1 μM of each metal ion were analyzed for acetate buffer within pH range from 2 to 9. The following initial test parameters were used: cleaning time = 15 s, cleaning potential = 1 V, deposition time = 250 s, deposition potential = -1.2 V, step size = 10 mV, and pulse width = 10 mV. The scanning range was maintained from -0.9 to 0.5 V to account for all the metal ion peaks.

The deposition potential was then varied and compared for each heavy metal ion across the range of -1.5 to 0.7 V. Lead shows a saturation plateau from -1.3 to -0.7 V with decreasing peak currents from then on (Figure 4B). Cadmium shows a similar plateau at -0.5 V and drops exponentially. Mercury shows a near constant peak current up to -0.1 V and peaks at 0.3 V before dropping exponentially. Hence, a deposition potential of -1.2 V seems ideal to get the optimal response for each heavy metal.

The scan rate was then varied from 10 to 100 mV/s (because each metal peak had an average peak potential region in a similar range) while keeping the previous two parameters constant. The peak intensity showed no change with minor peak broadening with an increasing scan rate. Keeping a scan rate beyond 100 mV/s caused instability in peak readings, and hence, the scan rate was maintained at 10 mV/s. The stripping scan rate affects only the resolution of peaks in the DPASV curve.

Herein, we compared the change in peak current with deposition time, as it determines the extent of THM incorporation into the Cu-TCPP MOF, resulting in a variation of the range and the limit of detection (LoD) of the electrode. Figure S4 shows the change in the peak current intensity in response to increasing preconcentration times of 1 μM doses of Pb^{2+} , Cd^{2+} , and Hg^{2+} . Each metal follows an exponential rise in peak current with deposition time increased in steps of 50 s from 50 to 500 s. Pb shows a regular exponential progression. However, the metals show no difference in amplitude up to 150 s until a sharp fall at 500 s followed by saturation possibly due to the exhaustion of available Cu sites. Three trials were conducted at 100, 250, and 450 s based on each region of the

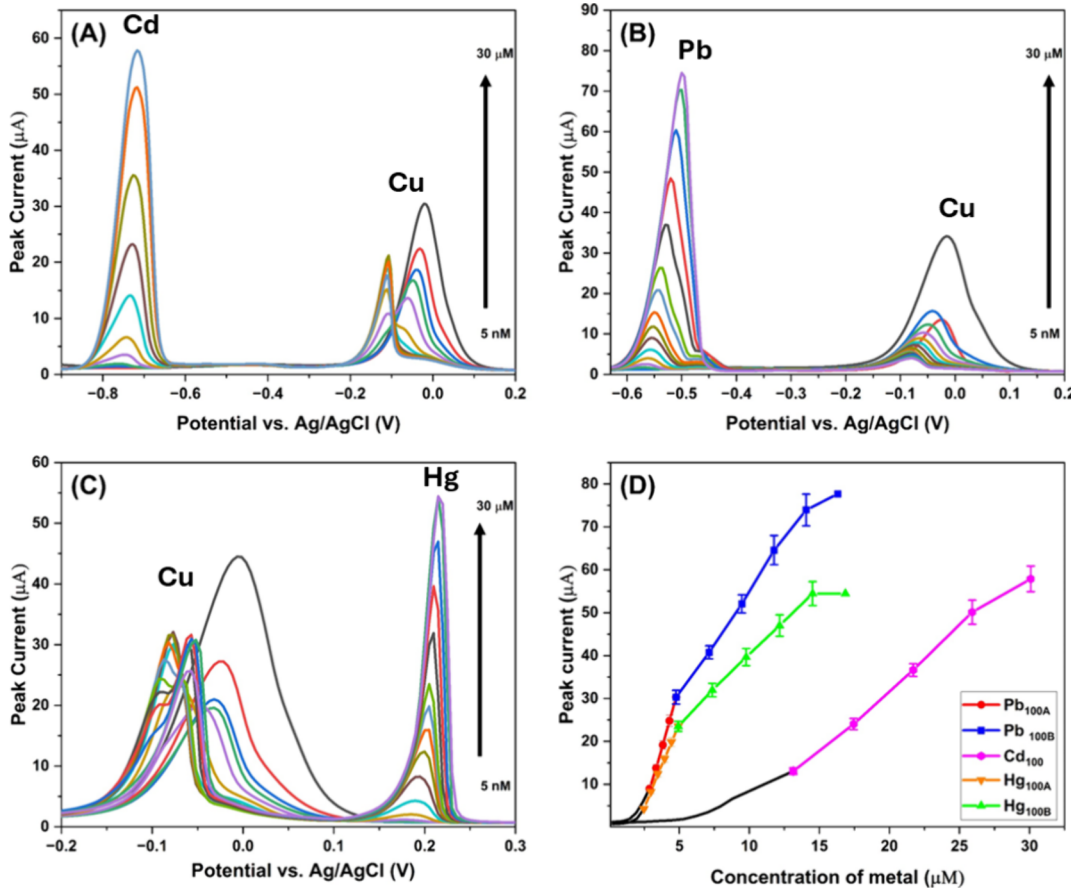


Figure 5. DPASV spectra for (A) cadmium, (B) lead, and (C) mercury and (D) calibration of peak currents vs metal concentration for each metal at 100 s accumulation time.

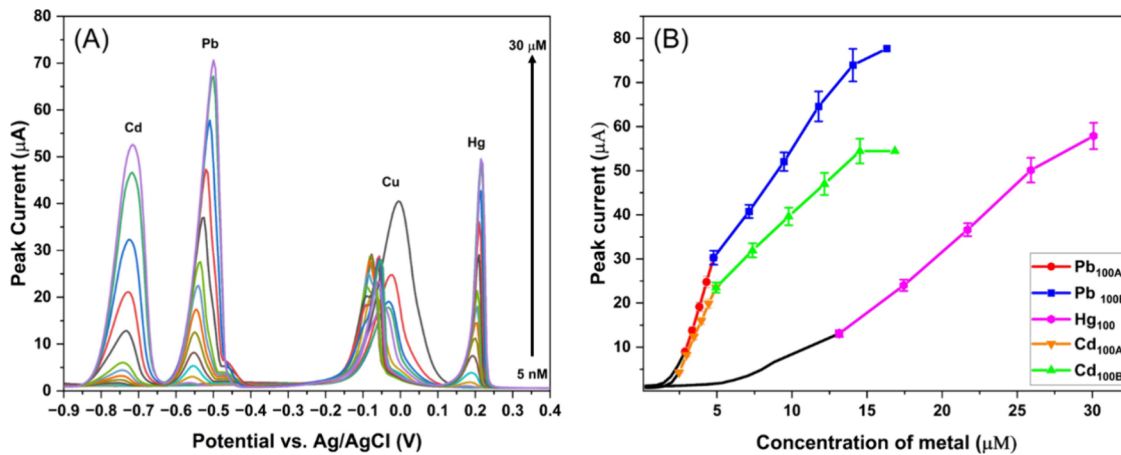


Figure 6. Multiplex THM-sensing DPASV data for 100 s of accumulation (A) and calibration and fitting (B).

optimization curve. The cleaning time was fixed at 30 s as there was no appreciable change in the Cu-TCPP behavior.

2.4. Effect of Deposition Time on Sensor Parameters.

Based on the lead deposition profile, three deposition times were chosen: 100, 250, and 450 s; these correspond to the linear, exponential, and peak zones as shown in Figure S4. We investigated each metal ion for its LoD and maximum range. The deposition was done at 100 s, and sensing is observed in the range 0.5–30 µM. As seen in Figure S5, lead showed the highest sensitivity at 0.5 µM, with two distinct linear zones, R1 and R2, and fitted with corresponding linear expressions (CM

= concentration of heavy metal in solution; IM = peak current of DPASV scan where M = Pb, Cd, or Hg). The high sensitivity and the sensing range are due to the lower activation energy in Cu-Pb intermetallics in comparison to other heavy metals.^{3,35} Lead replaces copper in the MOF, as seen in Figure SSA, where the copper response at -0.03 V diminishes when the lead content increases; this leads to the retention of only the central porphyrin copper with the lower peak at -0.1 V. The displaced copper does not seem to escape into the electrolyte due to the saturation of copper signals at higher lead concentrations. Cadmium shows a drastically lowered

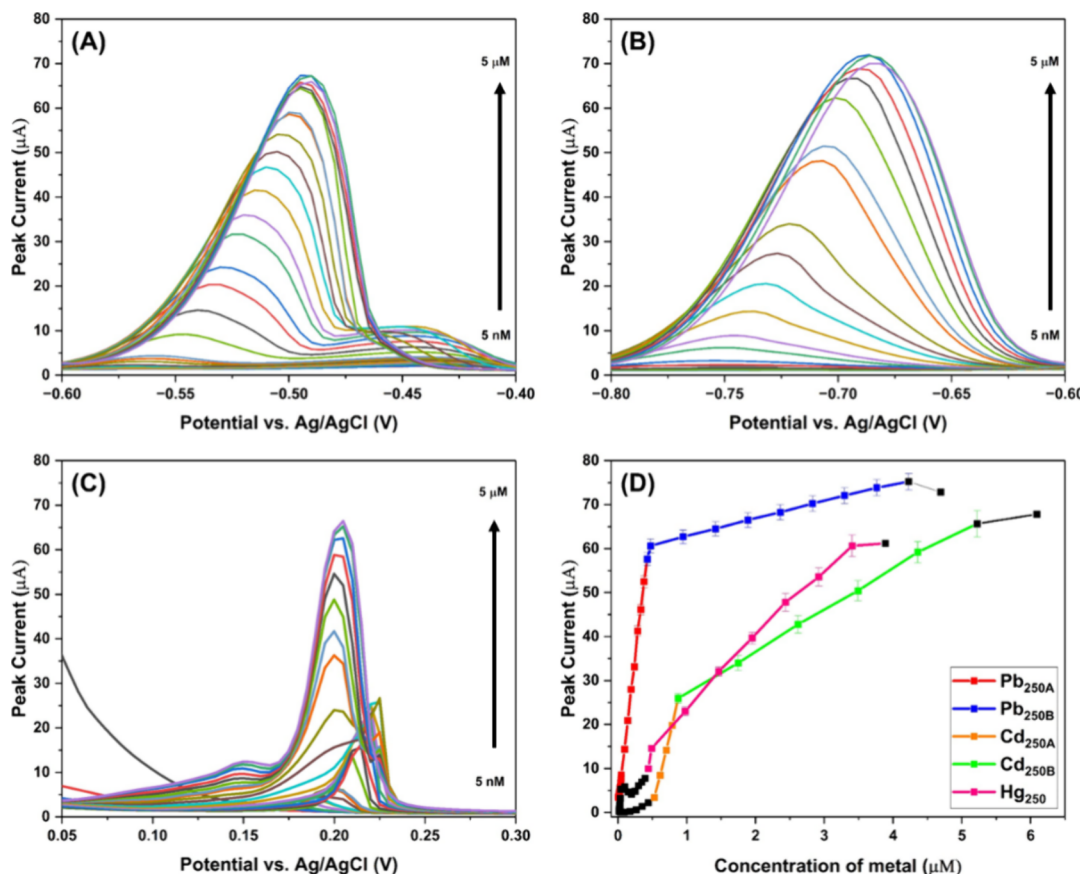


Figure 7. DPASV spectra for (A) lead, (B) cadmium, and (C) mercury, and (D) calibration of peak currents vs metal concentration for each metal at 250 s accumulation time.

LoD and range due to its 4d¹⁰ 5s² configuration. This leads to a semiexponential current response with a linear region from 13 to 26 μM of cadmium concentration. The presence of an increasing copper peak at -0.11V (Figure S6A) indicates the release of free Cu²⁺ into the electrolyte. Mercury showed a response that was similar to lead, although mercury's electronic configuration is similar to cadmium. This is due to the facile amalgamation of mercury with other metals.⁴³ Unlike lead, which replaces the Cu atoms in the MOF, mercury binds to copper metal nodes in configurations that are dependent on the copper concentration. Figure S7A shows three peaks in the copper response at 0.03, -0.11, and -0.057 V, which indicate the base state, free Cu²⁺, and Cu-Hg amalgam, respectively.

Akin to lead, mercury shows a bimodal response with two linear zones (Figure 5C,D), which matches the calibration equations in Table S3. The overall range shows a higher limit at 15 μM. We tabulated the results (Table S3) and observed that, at 100 s of deposition, mercury seems to show the best sensing characteristics with an LoD of 1.54 μM and a maximum range of 15 μM. All three metal solutions were then added to fresh sensing electrodes and analyzed for their simultaneous deposition profile.

We observed deposition profiles that were identical to those of the individual dosages that were superimposed on each other, as seen in Figure 6. The copper signal showed each of the three peaks that were observed for lead, cadmium, and mercury. The variation in copper response is due to the specific interaction mechanisms of the three metals with copper. The deposition time was then increased to 250 s, and the THM response was recorded. In consideration of this, lead

showed the lowest LoD at 4.3 nM at a maximum range of 4.25 μM (Figure S8A). Additionally, the appearance of the intermetallic peak at -0.43V is significant in this cycle owing to the longer deposition time. Apart from that, the combined signal of the -0.53 V Pb²⁺ peak and the -0.47 V Cu-Pb intermetallic yields a distinct bimodal calibration curve that is characterized by a low-concentration region (R1) and a high-concentration region (R2) with their respective fitting equations (Table S3: lead 250).

In response to cadmium, bimodal response is visible that is similar to lead, characterized with a higher LoD at 55 nM and the absence of an intermetallic zone (Figure S9A). The range is slightly higher at ~5.5 μM in the following calibration equations (Table S3: cadmium 250).

A dual redox process is observable in mercury at 250 s deposition. Three distinct peaks at 0.14, 0.19, and 0.225 V (Figure 7C) denote the Hg-Cu intermetallic and the two-step oxidation of Hg⁰ to Hg²⁺.³⁵



Figure S9B shows an increasing trend in the Hg¹⁺ oxidation, a decrease in the Hg²⁺ oxidation reaction at 0.225V, and an increase in Hg concentration indicating the saturation of Hg clusters on the Cu-TCPP surface and diffusion-dependent oxidative processes. This is attributed to the disintegration of the Cu-TCPP MOF after being tested for Hg. The anodic oxidation process, $\text{Hg} \rightarrow \text{Hg}^{2+} + 2\text{e}^-$, has a higher rate constant

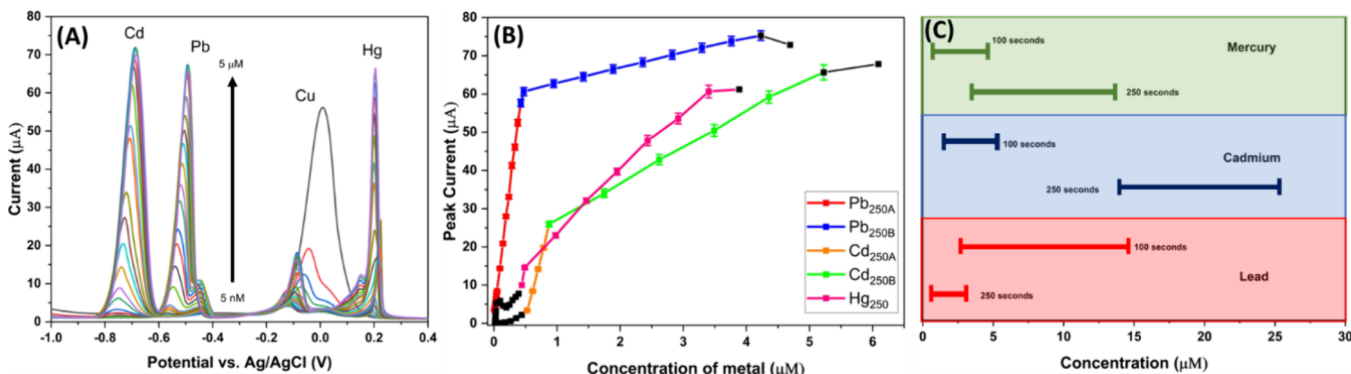


Figure 8. Multiplex-sensing trials for lead, cadmium, and mercury at 250 s of deposition (A). Specific metal DPASV responses (B) and range comparison (C).

than does the cathodic process, which results in higher peak currents, as observed in Figure 7C.³⁵ The combined peak currents for both oxidative processes yield the Hg response's true signal. Figure 7D shows only a single distinct linear range, from 0.5 to 3.5 μM, with an LoD of 0.45 μM. The calibration curve yields the fitting equation in Table S3 (Hg 250). Additionally, shoulder peaks are observed in Figure 7A–C at −0.45 and 0.15 V, respectively. These peaks are related to amalgam formations with copper by both lead and mercury. While the intensity of these peaks is significant at ~20% of the primary peak intensity, proper baseline considerations can eliminate the possible interference of these signals from the main oxidative peak, i.e., consider baselines only from −0.4 to −0.6 for lead for lead and 0.05 to 0.25 V for mercury.

In addition on conducting multiplex sensing of three metals in consideration, the observed responses are similar to that of individual metal sensing; this further proves the existence of different adsorption mechanisms for each metal ion on Cu-TCPP. In response to this, lead showed the lowest LoD at 4.5 nM, which is in line with American Public Health Association (APHA) guidelines for safe lead limits in drinking water.³⁶ A comparative table mentioning the LoD of existing heavy metal sensors with respect to the DNA-based biosensors is presented in the Supporting Information (Table S1) showing that the range is similar to that of inorganic carbon-based sensors already reported in previous models. Multiplex testing of all three heavy metals as seen in Figure 8 showed profiles identical with those of the individual metal testing titrations.

2.5. Interference and Reproducibility Studies. The selectivity of sensing materials to analytes in the presence of interferents is of high importance. Here, sensor selectivity and stability in high salt solutions and interfering counterions were studied by adding 10 μM of Pb²⁺, Cd²⁺, and Hg²⁺ to 10 mM solutions of Co²⁺, Ni²⁺, Na²⁺, K²⁺, Sn²⁺, and Zn²⁺. As seen in Figure 9, there appears to be a minor shifting of the Cu²⁺ peak on addition of each counterion in addition to a reduction in the peak current and an absence of any interferent peaks. This could be attributed to the surface adsorption of counterions without any chemical interactions, which further proves the robustness of the Cu-TCPP MOF to interference.^{37–40} Moreover, the addition of the tripartite metal solution to a fresh electrode yielded the expected response of Pb²⁺, Cd²⁺, and Hg²⁺ peaks. A study of tripartite sensing in the presence of counterions yielded a result within error margins of 10% and only a slight shifting of the Pb²⁺ peak.

Further, the response stability was proven by carrying out multiple studies of individual metal ion depositions and

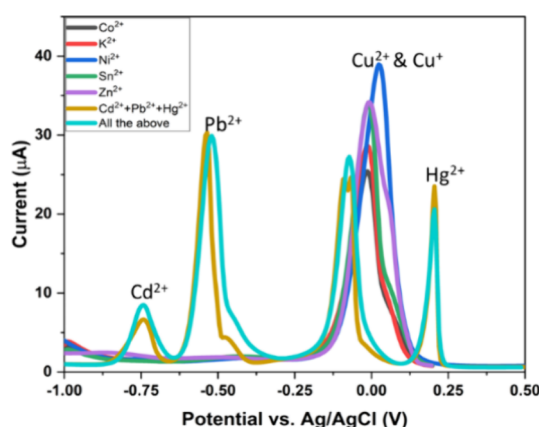


Figure 9. Interference trials for multiplex sensing of lead, cadmium, and mercury in the presence of interference ions.

checking the error margins. Three complete titrations with equimolar concentrations of Hg/Pb/Cd in a 1:1:1 ratio at each test concentration were analyzed using DPV and peak currents plotted as a titration curve. As seen in Figure 10a–c, low-concentration dosing yielded results that were almost identical with moderate error margins of ~10% at higher concentrations, which could be attributed to Cu-TCPP loading variations on the electrode. However, the electrode cannot be used more than once owing to the disintegration of long-range MOF coordination and replacement of Cu²⁺ ions with Pb²⁺, Cd²⁺, and Hg²⁺ ions that occur due to THM deposition (Figures S12 and S13).

2.6. Effect of THM on Cu-TCPP MOF. To study the chemical and morphological effects of chosen heavy metals on Cu-TCPP, the MOF was rinsed thoroughly with DI water, ethanol, and methanol three times and dried in a vacuum oven overnight before ion exchange with the THM solution. A solution of 5 mM of Pb(NO₃)₂ and Cd(NO₃)₂·4H₂O was dispersed in DI water and mixed with 1 μg/mL of the Cu-TCPP dispersion before it was sonicated at 700 Hz for 1 h and left to react for 12 h overnight. The dispersion was then centrifuged at 8000 rpm for 10 min and rinsed with DI water three times to remove any free ions; subsequently, the dispersion was dried overnight at 80 °C.

The characteristic Soret peaks⁴¹ of the Cu-TCPP seem to diminish upon the addition of specific THM salts (5 mM); subsequently, the peaks almost disappear with the tripartite addition of salts (Figure S13A). The presence of Pb seems to cause peak broadening, which is likely due to the presence of

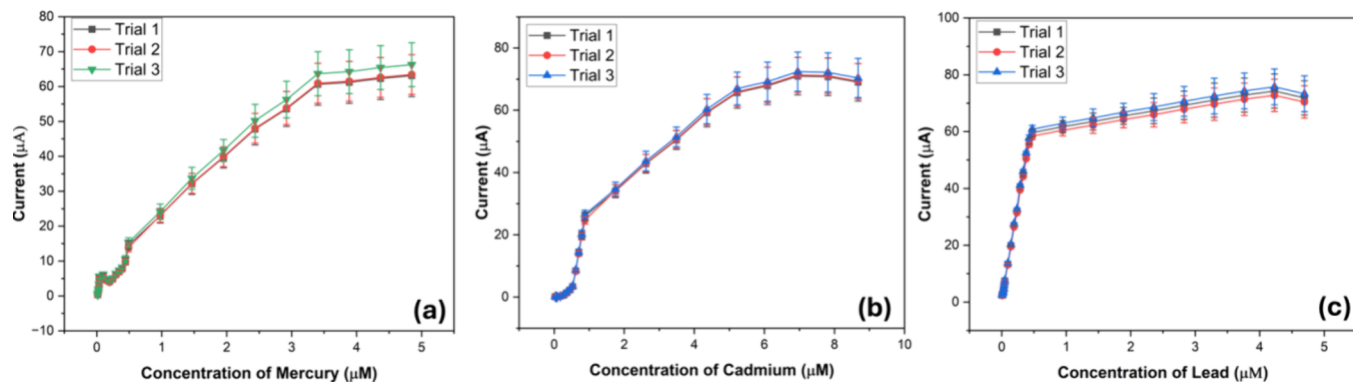


Figure 10. Reproducibility studies of multiplex sensing of each heavy metal ions as follows: (a) mercury, (b) cadmium, and (c) lead.

both Pb-TCPP and Cu-TCPP in both Soret peaks. Additionally, the same peak broadening occurs with a general reduction in the peak height on addition of THM salt addition. This can be explained by a net loss in the integrity of the MOF (Figure S13C) and is indicative of the influence of group 14 elements on the Cu-TCPP.

The chemical structure of the Cu-TCPP seems to be preserved in all cases, as seen in the FTIR spectra (Figure S13B) by the continued presence of the 1399 and 1602 cm^{-1} peaks. However, long-range order seems to have broken down, as seen in Figure S13C where the flake-like morphology is replaced by bulk sediments.

To identify the coordination of the MOF before and after THM exposure, XPS was performed on pure Cu-TCPP and Cu-TCPP exposed to THM. A suspension of Cu-TCPP was incubated with a solution of 5 μM of all heavy metal ions for 24 h, centrifuged, and rinsed with DI water three times to remove any dissolved salts before XPS. The presence of an intermetallic zone in the Cu 2p core level between $2\text{p}_{3/2}$ and $2\text{p}_{1/2}$ regions in Figure S12A proves the binding of lead to copper. The relative increase in the height of the Cu^{2+} deconvolution in the $\text{p}_{1/2}$ spectra also indicates that lead prefers to bind with copper.⁴² The presence of Pb4f , Hg4f , and Cd3d spectra indicates the adsorption and binding of heavy metals to the surface of the Cu-TCPP. The peaks at 150.4 and 153.5 eV show the divalent binding of Pb to the Cu-TCPP motif, similar to the low-intensity peak at 402.7 eV that shows Cd binding. The formation of metallic mercury clusters, owing to the deconvoluted peak at 98.7 eV and a weaker divalent binding peak at 99.45 eV, is displayed by Hg. Hence, interaction of THM with Cu-TCPP results in the loss of the long-range MOF structure and incorporation of Hg^{2+} , Pb^{2+} , and Cd^{2+} into the Cu^{2+} sites.

The structural integrity⁴³ of the Cu-TCPP MOF was investigated in further detail by running an XRD spectrum scan. As seen in Figure S13D, several of the XRD peaks seen earlier in Figure 2A have been retained with intensity differences. For example, the (110) intensity is higher post-THM exposure as well as the presence of an additional peak at 32 and 40°. Additionally, there are much higher background noise and smoothening of the peaks hinting at the possibility of an amorphous zone forming within the Cu-TCPP framework.

To conclude our above statements, ICP-OES studies of the solutions pre- and postexposure to MOF were done. Three solutions were tested: T1 = heavy metal solution containing approximately 250 ppb of Pb, 75 ppb of Hg, and 400 ppb of Cd (test solution); T2 = DI water mixed with Cu-TCPP,

stagnated for 24 h, sonicated, and centrifuged before testing (Cu standard); and T3 = test solution after exposure to Cu-TCPP MOF, cleaning, centrifugation, and ICP-OES analysis (filtrate). Table S3 shows the concentrations of Cu, Pb, Hg, and Cd for T1–T3. Cu content in the standard was present at a very low concentration, 11 ppb compared to the filtrate with a copper concentration of 141 ppb. Heavy metal concentrations in the filtrate T3 were much lower than those of the test solution T1. This indicates adsorption or binding of the heavy metals⁴⁴ on the Cu-TCPP unable to be removed even after sonication. Combined with the XPS data from Figure S12, we can safely conclude that copper from the MOF has been successfully exchanged with the heavy metals in the test solution.

3. REAL SAMPLE TESTING

The practical application of this electrode was demonstrated by testing it in predosed tap water and lake water samples (Powai Lake). Doses of 1 μM of Pb, Cd, and Hg were analyzed for $t_{\text{dep}} = 250$ s and tabulated with standardized testing results as seen in Figure 11.

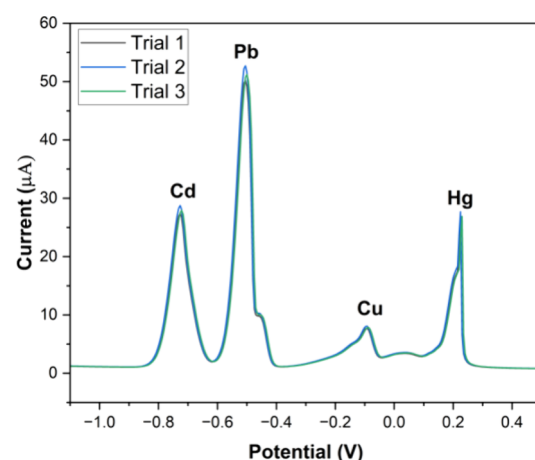


Figure 11. DPASV graphs of 1 μM Pb^{2+} , Cd^{2+} , and Hg^{+} in Powai Lake water spiked with acetate buffer.

The standard deviance and the quantitative recovery of the sensor were within the acceptable range (>95%), which imply that the Cu-TCPP sensor is relevant to tripartite heavy metal detection in real-world samples (Table S2). Each individual metal ion peak for the test samples is tabulated in Table S5, with mean, standard deviation, and coefficient of variation %.

We note that the CV% is < 5%, making it an acceptable first test case study for this electrode to be used in future devices for electrochemical sensing of heavy metal ions. However, we must also note that further tests done in tap water and industrial effluent need to be done to ensure proper calibration in actual device applications.

4. CONCLUSIONS

In this study, we have successfully investigated and characterized a Cu-TCPP MOF for the electrochemical detection of toxic heavy metals (THM) in water, yielding valuable insights into the design, optimization, and application of this novel sensing material. The synthesized MOF demonstrated its unique "paddle-wheel" structure characterized by a large surface area and high-density active metal sites displaying a layered nanoflake structure, offering increased interaction for electrode applications. DPASV deposition time optimization allowed us to fine-tune the sensor's sensitivity and range for different heavy metals, namely, Pb, Cd, and Hg. The resulting calibration curves highlighted distinct response patterns for each metal, offering the potential for multiplex THM detection. Lead sensing shows the best promise due to the lowest LoD of 5 nm at 250 s deposition time. Selectivity tests in the presence of interfering ions and stability assessments in high-salt solutions confirmed the robustness of the Cu-TCPP sensor. Reproducibility studies indicated the electrode's reliability, although it is limited to a single use due to MOF disintegration upon long THM exposure. Our investigation into the chemical and morphological effects of THMs on the Cu-TCPP MOF provided crucial insights. Changes in UV-vis, FTIR, and morphology indicated the influence of THMs on the MOF integrity, with evidence of heavy metal binding. Practical application tests in predosed tap water and lake water samples validated the sensor's efficacy in real-world scenarios. The sensor exhibited quantitative recovery and stability, reinforcing its relevance for tripartite heavy metal detection in environmental samples. Overall, this research represents a significant contribution to the fields of environmental science and sensor technology. The study of the Cu-TCPP MOF as a heavy metal sensor with versatile applicability and selectivity showcases its potential for addressing critical challenges related to THM contamination. As we continue to refine and expand the capabilities of this material, it holds promise for the early detection and monitoring of THMs, thereby contributing to the protection of our ecosystems and public health. Future work will focus on making a portable and freestanding sensing device based on Cu-TCPP without the need for a laboratory setup and exploring additional applications in environmental monitoring and beyond.

■ ASSOCIATED CONTENT

SI Supporting Information

The Supporting Information is available free of charge at <https://pubs.acs.org/doi/10.1021/acsami.4c12974>.

Materials and synthesis methods including the fabrication of electrochemical cell used in the analysis; XPS figures of pristine Cu-TCPP; cyclic voltammetry calibration of Cu-TCPP in acetate buffer; calibration of the tripartite metal sensing graphs and fitting; table of electrode comparison with existing metal sensing devices; morphological changes in Cu-TCPP after

THM exposure; XPS spectra of Cu-TCPP postexposure; and table of comparison of real water sample testing comparison ([PDF](#))

■ AUTHOR INFORMATION

Corresponding Author

Prashanth Kannan – IITB-Monash Research Academy, IIT Bombay, Mumbai, Maharashtra 400076, India;
Email: Prashanth.kannan@monash.edu

Authors

Ajay Narayan Konda Ravindranath – Department of Metallurgical Engineering and Materials Science, IIT Bombay, Mumbai, Maharashtra 400076, India

Sunil Suresh Domala – Department of Metallurgical Engineering and Materials Science, IIT Bombay, Mumbai, Maharashtra 400076, India

Mitko Oldfield – School of Physics and Astronomy and ARC Centre of Excellence in Future Low-Energy Electronics Technologies, Monash University, Clayton, VIC 3800, Australia

Agustin Schiffrin – School of Physics and Astronomy and ARC Centre of Excellence in Future Low-Energy Electronics Technologies, Monash University, Clayton, VIC 3800, Australia; orcid.org/0000-0003-1140-8485

Dipti Gupta – Department of Metallurgical Engineering and Materials Science, IIT Bombay, Mumbai, Maharashtra 400076, India; orcid.org/0000-0003-3252-3407

Complete contact information is available at:

<https://pubs.acs.org/10.1021/acsami.4c12974>

Author Contributions

The manuscript was written through contributions of all authors. All authors have given approval to the final version of the manuscript. P.K. designed, performed, and conceived the experiment including the bulk of the analysis and writing the paper. S.S.D. and A.N. contributed to experimental analysis and writing and proof-reading of the paper. M.O. assisted with the UV-vis spectra of TCPP.

Funding

This project was completed with the assistance of funding given by the Department of Biotechnology (DBT), Govt. of India. This work is also supported by the "Water Technology Initiative 2023".

Notes

The authors declare no competing financial interest.

■ ACKNOWLEDGMENTS

All electrochemical measurements were carried out at the PEEL Lab, IIT Bombay, and supported by the Department of Biotechnology (DBT), Government of India. M.O. performed and analyzed UV-vis spectra. A.N. and S.S.D. assisted with electrochemical data gathering and analysis. [Figure 1](#) was made using the Biorender and Avogadro software. All authors declare that they have no competing interests. All data needed to evaluate the conclusions in this paper are present in the paper and/or in the SI. A.S. acknowledges the financial support from the Australian Research Council Centre of Excellence in Future Low-Energy Electronics Technologies (CE170100039). P.K., A.S., and D.G. acknowledge the financial support from the IITB-Monash Research Academy.

■ ABBREVIATIONS

TCPP=tetrakis(4-carboxyphenyl)porphyrin
MOF=metal–organic framework
THM=toxic heavy metals
DPASV=differential pulse anodic stripping voltammetry
LoD=limit of detection
XPS=X-ray photoelectrolyt spectroscopy
ICP-OES=inductively coupled plasma optical emission spectroscopy
FTIR=Fourier transform infrared spectroscopy

■ REFERENCES

- (1) Arti; Mehra, R. Analysis of heavy metals and toxicity level in the tannery effluent and the environs. *Environ. Monit. Assess.* **2023**, *195* (5), 554.
- (2) Zheng, K.; Zeng, Z.; Tian, Q.; Huang, J.; Zhong, Q.; Huo, X. Epidemiological evidence for the effect of environmental heavy metal exposure on the immune system in children. *Sci. Total Environ.* **2023**, *868*, No. 161691.
- (3) Wei, Y.; Gao, C.; Meng, F. L.; Li, H.-H.; Wang, L.; Liu, J.-H.; Huang, X.-J. SnO₂/Reduced Graphene Oxide Nanocomposite for the Simultaneous Electrochemical Detection of Cadmium(II), Lead(II), Copper(II), and Mercury(II): An Interesting Favorable Mutual Interference. *J. Phys. Chem. C* **2012**, *116* (1), 1034–1041.
- (4) Zhu, G.; Ge, Y.; Dai, Y.; Shang, X.; Yang, J.; Liu, J. Size-tunable polyaniline nanotube-modified electrode for simultaneous determination of Pb(II) and Cd(II). *Electrochim. Acta* **2018**, *268*, 202–210.
- (5) Pulgarín, J. A.; Bermejo, L. F.; Durán, A. C. Fast simultaneous determination of traces of Cu(II) and Co(II) in soils and sediments with the luminol/perborate chemiluminescent system. *Environ Monit Assess.* **2013**, *185* (1), 573–80.
- (6) Veerakumar, P.; Veeramani, V.; Chen, S.-M.; Madhu, R.; Liu, S.-B. Palladium Nanoparticle Incorporated Porous Activated Carbon: Electrochemical Detection of Toxic Metal Ions. *ACS Appl. Mater. Interfaces* **2016**, *8* (2), 1319–1326.
- (7) Thatikayala, D.; Noori, M. T.; Min, B. Zeolite-modified electrodes for electrochemical sensing of heavy metal ions – Progress and future directions. *Materials Today Chemistry* **2023**, *29*, No. 101412.
- (8) Gongi, W.; Rube, M.; Ben Ouada, H.; Ben Ouada, H.; Tamarin, O.; Dejous, C. Elaboration and Characterization of a New Heavy Metal Sensor Functionalized by Extracellular Polymeric Substances Isolated from a Tunisian Thermophilic Microalga Strain Graesiella sp. *Sensors* **2023**, *23*, 803.
- (9) Naseri, M.; Mohammadniaei, M.; Ghosh, K.; Sarkar, S.; Sankar, R.; Mukherjee, S.; Pal, S.; Ansari Dezfooli, E.; Halder, A.; Qiao, J.; Bhattacharyya, N.; Sun, Y. A Robust Electrochemical Sensor Based on Butterfly-shaped Silver Nanostructure for Concurrent Quantification of Heavy Metals in Water Samples. *Electroanalysis* **2023**, *35*, No. e202200114.
- (10) Sandoval Bojórquez, D. I.; Janićjević, Ž.; Palestina Romero, B.; Oliveros Mata, E. S.; Laube, M.; Feldmann, A.; Kegler, A.; Drewitz, L.; Fowley, C.; Pietzsch, J.; Fassbender, J.; Tonn, T.; Bachmann, M.; Baraban, L. Impedimetric Nanobiosensor for the Detection of SARS-CoV-2 Antigens and Antibodies. *ACS Sens.* **2023**, *8* (2), 576–586.
- (11) Dai, Y.; Molazemhosseini, A.; Liu, C. C. A Single-Use, In Vitro Biosensor for the Detection of T-Tau Protein, A Biomarker of Neuro-Degenerative Disorders, in PBS and Human Serum Using Differential Pulse Voltammetry (DPV). *Biosensors (Basel.)* **2017**, *7* (1), 10.
- (12) Sabah, M.; Fethi, A. Electrochemical Detection of Lead in Real Samples Using Carbon Nanostructure and Inactivated *E. coli* as Low-Cost Sensitive Biosensor with High Electrocatalytic Performance. *Electrocatalysis* **2022**, *13*, 773–783.
- (13) Cui, G.; Kim, S. J.; Choi, S. H.; Nam, H.; Cha, G. S.; Paeng, K. J. A disposable amperometric sensor screen printed on a nitrocellulose strip: a glucose biosensor employing lead oxide as an interference-removing agent. *Anal. Chem.* **2000**, *72* (8), 1925–1929.
- (14) Wan, J.; Shen, Y.; Xu, L.; Xu, R.; Zhang, J.; Sun, H.; Zhang, C.; Yin, C.; Wang, X. Ferrocene-functionalized Ni(II)-based metal-organic framework as electrochemical sensing interface for ratiometric analysis of Cu²⁺, Pb²⁺ and Cd²⁺. *J. Electroanal. Chem.* **2021**, *895*, No. 115374.
- (15) Ma, L.; Zhang, X.; Ikram, M.; Ullah, M.; Wu, H.; Shi, K. Controllable synthesis of an intercalated ZIF-67/EG structure for the detection of ultratrace Cd²⁺, Cu²⁺, Hg²⁺ and Pb²⁺ ions. *Chem. Eng. J.* **2020**, *395*, No. 125216.
- (16) Liu, C.; Wang, J.; Wan, J.; Yu, C. MOF-on-MOF hybrids: Synthesis and applications. *Coord. Chem. Rev.* **2021**, *432*, No. 213743.
- (17) Freund, R.; Zaremba, O.; Arnauts, G.; Ameloot, R.; Skorupskii, G.; Dincă, M.; Bavykina, A.; Gascon, J.; Ejsmont, A.; Goscianska, J.; Kalmutzki, M.; Lächelt, U.; Ploetz, E.; Diercks, C. S.; Wuttke, S. *Angew. Chem., Int. Ed.* **2021**, *60*, 23975.
- (18) Choi, J. Y.; Wang, M.; Check, B.; Stodolka, M.; Tayman, K.; Sharma, S.; Park, J. Linker-Based Bandgap Tuning in Conductive MOF Solid Solutions. *Small* **2023**, *19*, No. 2206988.
- (19) Yi, S.; Shi, W.; Yang, X.; Yao, Z. Engineering sensitive gas sensor based on MOF-derived hollow metal-oxide semiconductor heterostructures. *Talanta* **2023**, *258*, No. 124442.
- (20) Noorani, N.; Mehrdad, A. Improving performance of mesoporous MOF AlTp impregnated with ionic liquids for CO₂ adsorption. *Sci. Rep.* **2023**, *13*, 3227.
- (21) Lu, Y.; Lin, S.; Cao, H.; Xia, Y.; Xia, Y.; Xin, L.; Qu, K.; Zhang, D.; Yu, Y.; Huang, K.; Jing, W.; Xu, Z. Efficient proton-selective hybrid membrane embedded with polydopamine modified MOF-808 for vanadium flow battery. *J. Membr. Sci.* **2023**, *671*, No. 121347.
- (22) Gunaseelan, H.; Munde, A. V.; Patel, R.; Sathe, B. R. Metal-organic framework derived carbon-based electrocatalysis for hydrogen evolution reactions: A review. *Materials Today Sustainability* **2023**, *22*, No. 100371.
- (23) Guo, J.; Liang, Y.; Liu, L.; Hu, J.; Wang, H.; An, W.; Cui, W. Noble-metal-free CdS/Ni-MOF composites with highly efficient charge separation for photocatalytic H₂ evolution. *Appl. Surf. Sci.* **2020**, *522*, No. 146356.
- (24) El-Binary, M. A.; Shahat, A.; El-Deen, I. M.; El-Afify, M. A. M.; Hassan, N. Synthesis of novel fluorescent sensor based on a modified amino Al-MOF for rapid, sensitive, and selective detection of arsenic in aqueous solution. *Appl. Organomet. Chem.* **2023**, *37* (6), No. e7102.
- (25) Zhao, J.; Long, Y.; He, C.; Yang, H.; Zhao, S.; Luo, X.; Huo, D.; Hou, C. Simultaneous Electrochemical Detection of Cd²⁺ and Pb²⁺ Based on an MOF-Derived Carbon Composite Linked with Multiwalled Carbon Nanotubes. *ACS Sustainable Chem. Eng.* **2023**, *11* (6), 2160–2171.
- (26) Li, P.; Chen, X.; Guo, C.; Zou, H.; Chen, Z.; Liu, B.; Liang, W.; Cai, J.; Xu, H. A Logic Fluorescent Chemosensor Based on Eu³⁺-Functionalized Cd-MOFs for Sensing Fe³⁺ and Cu²⁺ Synchronously. *Eur. J. Inorg. Chem.* **2023**, *26*, No. e202200576.
- (27) Liang, Q.; Xiao, W.; Zhang, C.; Zhu, D.; Wang, S.-L.; Tian, S.-Y.; Long, T.; Yue, E.-L.; Wang, J.-J.; Hou, X.-Y. MOFs-based Fe@YAU-101/GCE electrochemical sensor platform for highly selective detecting trace multiplex heavy metal ions. *Talanta* **2023**, *259*, No. 124491.
- (28) Hu, R.; Zhang, X.; Chi, K.-N.; Yang, T.; Yang, Y.-H. Bifunctional MOFs-Based Ratiometric Electrochemical Sensor for Multiplex Heavy Metal Ions. *ACS Appl. Mater. Interfaces* **2020**, *12* (27), 30770–30778.
- (29) Zhao, M.; Wang, Y.; Ma, Q.; Huang, Y.; Zhang, X.; Ping, J.; Zhang, Z.; Lu, Q.; Yu, Y.; Xu, H.; Zhao, Y.; Zhang, H. Ultrathin 2D Metal–Organic Framework Nanosheets. *Adv. Mater.* **2015**, *27*, 7372–7378.
- (30) Song, Y.; Sun, Y.; Du, D.; Zhang, M.; Liu, Y.; Liu, L.; Ji, T.; He, G.; Liu, Y. Fabrication of c-oriented ultrathin TCPP-derived 2D MOF membrane for precise molecular sieving. *J. Membr. Sci.* **2021**, *634*, No. 119393.
- (31) Hussain, S.; Deng, Z.; Khan, A.; Li, P.; Li, Z.; Fang, Z.; Wan, X.; Peng, X. Photothermal responsive ultrathin Cu-TCPP nanosheets/

sulfonated polystyrene nanocomposite photo-switch proton conducting membranes. *J. Membr. Sci.* **2021**, *620*, No. 118888.

(32) Rahimi, R.; Shariatinia, S.; Zargari, S.; Yaghoubi Berijani, M.; Ghaffarinejad, A.; Shojaie, Z. S. Synthesis, characterization, and photocurrent generation of a new nanocomposite based Cu–TCPP MOF and ZnO nanorod. *RSC Adv.* **2015**, *5*, 46624–46631.

(33) Lee, D. T.; Jamir, J. D.; Peterson, G. W.; Parsons, G. N. Water-Stable Chemical-Protective Textiles via Euhedral Surface-Oriented 2D Cu-TCPP Metal-Organic Frameworks. *Small.* **2019**, *15* (10), No. e1805133.

(34) Elgrishi, N.; Rountree, K. J.; McCarthy, B. D.; Rountree, E. S.; Eisenhart, T. T.; Dempsey, J. L. A Practical Beginner's Guide to Cyclic Voltammetry. *J. Chem. Educ.* **2018**, *95* (2), 197–206.

(35) Shtepliuk, I.; Vagin, M.; Yakimova, R. Insights into the Electrochemical Behavior of Mercury on Graphene/SiC Electrodes. *C* **2019**, *5*, 51.

(36) Kumar, M.; Puri, A. A review of permissible limits of drinking water. *Indian J Occup Environ Med.* **2012**, *16* (1), 40–4.

(37) Xu, K.; Pérez-Ràfols, C.; Marchoud, A.; Cuartero, M.; Crespo, G. A. Anodic Stripping Voltammetry with the Hanging Mercury Drop Electrode for Trace Metal Detection in Soil Samples. *Chemosensors* **2021**, *9*, 107.

(38) Xu, X.; Duan, G.; Li, Y.; Liu, G.; Wang, J.; Zhang, H.; Dai, Z.; Cai, W. Fabrication of gold nanoparticles by laser ablation in liquid and their application for simultaneous electrochemical detection of Cd²⁺, Pb²⁺, Cu²⁺, Hg²⁺. *ACS Appl. Mater. Interfaces* **2014**, *6*, 65–71.

(39) Lu, M.; Deng, Y.; Luo, Y.; Lv, J.; Li, T.; Xu, J.; Chen, S.-W.; Wang, J. Graphene aerogel–metal–organic framework-based electrochemical method for simultaneous detection of multiple heavy-metal ions. *Anal. Chem.* **2019**, *91*, 888–895.

(40) Gao, F.; Gao, N.; Nishitani, A.; Tanaka, H. Rod-like hydroxyapatite and Nafion nanocomposite as an electrochemical matrix for simultaneous and sensitive detection of Hg²⁺, Cu²⁺, Pb²⁺ and Cd²⁺. *J. Electroanal. Chem.* **2016**, *775*, 212–218.

(41) Sang, S.; Li, D.; Zhang, H.; Sun, Y.; Jian, A.; Zhang, Q.; Zhang, W. Facile synthesis of AgNPs on reduced graphene oxide for highly sensitive simultaneous detection of heavy metal ions. *RSC Adv.* **2017**, *7*, 21618–21624.

(42) Ganiga, M.; Cyriac, J. Understanding the Photoluminescence Mechanism of Nitrogen-Doped Carbon Dots by Selective Interaction with Copper Ions. *ChemPhysChem* **2016**, *17*, 2315.

(43) Sakamoto, M.; Nakamura, M.; Murata, K. [Mercury as a Global Pollutant and Mercury Exposure Assessment and Health Effects]. *Nihon Eiseigaku zasshi. Japanese Journal of Hygiene.* **2018**, *73* (3), 258–264.

(44) Van Staden, J.; Matoetoe, M. Simultaneous determination of copper, lead, cadmium and zinc using differential pulse anodic stripping voltammetry in a flow system. *Anal. Chim. Acta* **2000**, *411*, 201–207.